

# Reactivity of a Cobalt(III)–Hydroperoxy Complex in Electrophilic Reactions

Bongki Shin,<sup>†</sup> Kyle D. Sutherlin,<sup>‡</sup> Takehiro Ohta,<sup>§</sup> Takashi Ogura,<sup>§</sup> Edward I. Solomon,<sup>\*,‡,||</sup> and Jaeheung Cho<sup>\*,†</sup>

<sup>†</sup>Department of Emerging Materials Science, DGIST, Daegu 42988, Korea

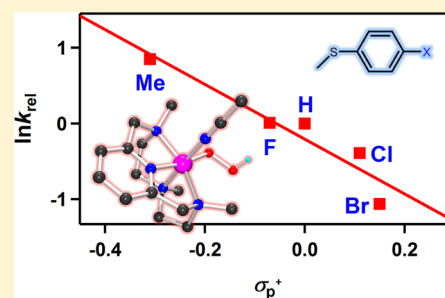
<sup>‡</sup>Department of Chemistry, Stanford University, Stanford, California 94305, United States

<sup>§</sup>Picobiology Institute, Graduate School of Life Science, University of Hyogo, RSC-UH LP Center, Hyogo 679-5148, Japan

<sup>||</sup>Stanford Synchrotron Radiation Laboratory, Stanford Linear Accelerator Center, Menlo Park, California 94025, United States

## Supporting Information

**ABSTRACT:** The reactivity of mononuclear metal–hydroperoxy adducts has fascinated researchers in many areas due to their diverse biological and catalytic processes. In this study, a mononuclear cobalt(III)–peroxy complex bearing a tetradentate macrocyclic ligand,  $[\text{Co}^{\text{III}}(\text{Me}_3\text{-TPADP})(\text{O}_2)]^+$  ( $\text{Me}_3\text{-TPADP}$  = 3,6,9-trimethyl-3,6,9-triaza-1(2,6)-pyridinacyclodecaphane), was prepared by reacting  $[\text{Co}^{\text{II}}(\text{Me}_3\text{-TPADP})(\text{CH}_3\text{CN})_2]^{2+}$  with  $\text{H}_2\text{O}_2$  in the presence of triethylamine. Upon protonation, the cobalt(III)–peroxy intermediate was converted into a cobalt(III)–hydroperoxy complex,  $[\text{Co}^{\text{III}}(\text{Me}_3\text{-TPADP})(\text{O}_2\text{H})(\text{CH}_3\text{CN})]^{2+}$ . The mononuclear cobalt(III)–peroxy and –hydroperoxy intermediates were characterized by a variety of physicochemical methods. Results of electrospray ionization mass spectrometry clearly show the transformation of the intermediates: the peak at  $m/z$  339.2 assignable to the cobalt(III)–peroxy species disappears with concomitant growth of the peak at  $m/z$  190.7 corresponding to the cobalt(III)–hydroperoxy complex (with bound  $\text{CH}_3\text{CN}$ ). Isotope labeling experiments further support the existence of the cobalt(III)–peroxy and –hydroperoxy complexes. In particular, the O–O bond stretching frequency of the cobalt(III)–hydroperoxy complex was determined to be  $851\text{ cm}^{-1}$  for  $^{16}\text{O}_2\text{H}$  samples ( $803\text{ cm}^{-1}$  for  $^{18}\text{O}_2\text{H}$  samples), and its Co–O vibrational energy was observed at  $571\text{ cm}^{-1}$  for  $^{16}\text{O}_2\text{H}$  samples ( $551\text{ cm}^{-1}$  for  $^{18}\text{O}_2\text{H}$  samples;  $568\text{ cm}^{-1}$  for  $^{16}\text{O}_2^2\text{H}$  samples) by resonance Raman spectroscopy. Reactivity studies performed with the cobalt(III)–peroxy and –hydroperoxy complexes in organic functionalizations reveal that the latter is capable of conducting oxygen atom transfer with an electrophilic character, whereas the former exhibits no oxygen atom transfer reactivity under the same reaction conditions. Alternatively, the cobalt(III)–hydroperoxy complex does not perform hydrogen atom transfer reactions, while analogous low-spin Fe(III)–hydroperoxy complexes are capable of this reactivity. Density functional theory calculations indicate that this lack of reactivity is due to the high free energy cost of O–O bond homolysis that would be required to produce the hypothetical Co(IV)–oxo product.



## INTRODUCTION

Mononuclear metal–oxygen species such as metal–superoxo, –peroxy, –hydroperoxy, and –oxo complexes have important roles as key intermediates involved in catalytic oxygenation reactions and biological oxidation reactions.<sup>1–5</sup> Heme and nonheme iron–oxygen intermediates have been invoked in the catalytic cycles of dioxygen activation by metalloenzymes.<sup>6</sup> Among the iron–oxygen adducts, iron–hydroperoxy species have received considerable attention, since the intermediates have been implicated as reactive species in DNA cleavage activity of bleomycin, a glycopeptide that is effective as an antitumor drug in concert with iron and dioxygen.<sup>7</sup>

In the case of cobalt complexes, a large number of cobalt– $\text{O}_2$  species have been synthesized as models of dioxygen carrier proteins and as oxidants in organic functionalizations.<sup>8,9</sup> In models of biological oxygen carriers, Cavin et al., for example, have extensively examined the oxygen carrier properties of

cobalt(II) complexes with SALEN ligands.<sup>10</sup> In addition, the synthetic complexes have potential applications in dioxygen separation and storage.<sup>11</sup>

Recent advances in the characterization and reactivity of cobalt– $\text{O}_2$  intermediates reveal that the cobalt–superoxo and –peroxy species are active oxidants in electrophilic and nucleophilic reactions.<sup>12</sup> A notable example is the formation of side-on cobalt(III)–peroxy complexes bearing a series of tetraazamacrocyclic ligands.<sup>8a,c</sup> The intermediates have nucleophilic character (e.g., aldehyde deformylation) toward organic substrates. The end-on cobalt(III)–superoxo species has been proposed as reactive species in electrophilic reactions (e.g., hydrogen atom transfer).<sup>13</sup> Very recently, the reactivity of an end-on cobalt(II)–superoxo intermediate with a redox non-

Received: September 22, 2016



$C_{18}H_{30}Cl_2CoN_6O_8$ , monoclinic,  $P2_1/n$ ,  $Z = 8$ ,  $a = 15.7400(3)$  Å,  $b = 19.7237(4)$  Å,  $c = 16.3257(3)$  Å,  $\beta = 97.6290(10)^\circ$ ,  $V = 5023.47(17)$  Å<sup>3</sup>,  $\mu = 0.951$  mm<sup>-1</sup>,  $\rho_{\text{calcd}} = 1.556$  g/cm<sup>3</sup>,  $R1 = 0.0345$ ,  $wR2 = 0.0890$  for 12456 unique reflections, 641 variables. The crystallographic data for  $[Co^{II}(Me_3\text{-TPADP})(CH_3CN)_2](ClO_4)_2$  is listed in Table S1, and Table S2 lists the selected bond distances and angles. CCDC-1448782 for  $[Co^{II}(Me_3\text{-TPADP})(CH_3CN)_2](ClO_4)_2$  contains the supplementary crystallographic data for this paper. These data can be obtained free of charge via [www.ccdc.cam.ac.uk/data\\_request/cif](http://www.ccdc.cam.ac.uk/data_request/cif) (or from the Cambridge Crystallographic Data Centre, 12, Union Road, Cambridge CB2 1EZ, U.K.; fax (+44) 1223-336-033; or e-mail [deposit@ccdc.cam.ac.uk](mailto:deposit@ccdc.cam.ac.uk)).

**Computational Details.** DFT calculations were performed using the Gaussian 09 computational package.<sup>21</sup> All calculations used the B3LYP functional and the TZVP basis, and solvent effects were included using the polarized continuum model with acetonitrile as the solvent. Geometry optimizations were carried out using the default convergence criteria and were confirmed as minima by the absence of imaginary modes in a frequency calculation. Enthalpies and Gibbs free energies were calculated at 298.15 K. Mayer bond order analysis was performed using QMForge,<sup>22</sup> and molecular orbital contours were obtained using LUMO.<sup>23</sup>

**Reactivity Studies.** All reactions were run monitoring UV–vis spectral changes of reaction solutions, and rate constants were determined by fitting the changes in absorbance at 523 nm for  $[Co^{III}(Me_3\text{-TPADP})(O_2H)(CH_3CN)]^{2+}$  (3). Reactions were run at least in triplicate, and the data reported represent the average of these reactions. *In-situ*-generated 3 was used in kinetic studies, such as the oxidation of triphenylphosphine (PPh<sub>3</sub>) and thioanisole in CH<sub>3</sub>CN at –20 and –40 °C. After the completion of reactions, pseudo-first-order fitting of the kinetic data allowed us to determine  $k_{\text{obs}}$  values. Products formed in the oxidation of PPh<sub>3</sub> by 3 in CH<sub>3</sub>CN at –20 °C were analyzed by <sup>31</sup>P NMR. Products formed in the oxidation of thioanisole by 3 in CH<sub>3</sub>CN at –20 °C were analyzed by injecting the reaction mixture directly into GC and GC–MS. Products were identified by comparison with authentic samples, and product yields were determined by comparison against standard curves prepared with authentic samples.

## RESULTS AND DISCUSSION

**Synthesis and Characterization.** Me<sub>3</sub>-TPADP was synthesized by a modification of a previously reported procedure [see the Experimental Section in the Supporting Information (SI)].<sup>24</sup> The Me<sub>3</sub>-TPADP was characterized by electrospray ionization mass spectrometry (ESI-MS) and <sup>1</sup>H and <sup>13</sup>C nuclear magnetic resonance (NMR) methods (see the SI Experimental Section).

Synthetic procedures for Co(II) and Co(III) complexes used are outlined in Scheme 2. The purple starting Co(II) complex,  $[Co^{II}(Me_3\text{-TPADP})(CH_3CN)_2](ClO_4)_2$  (1-(ClO<sub>4</sub>)<sub>2</sub>), was synthesized by reacting  $Co(ClO_4)_2 \cdot 6H_2O$  with the Me<sub>3</sub>-TPADP ligand in CH<sub>3</sub>CN. Single crystals of 1-(ClO<sub>4</sub>)<sub>2</sub> contained two crystallographically independent but virtually identical cations in the asymmetric unit (denoted “A” and “B”; see the SI, Tables S1 and S2). Complex 1 has a six-coordinated Co(II) ion with four nitrogen atoms of the Me<sub>3</sub>-TPADP ligand and two nitrogen atoms of CH<sub>3</sub>CN solvent molecules (Figure 1a). The Co(II) geometry is best described as a distorted octahedral.

The UV–vis spectrum of 1 in CH<sub>3</sub>CN shows a broad absorption band at 498 nm ( $\epsilon = 80$  M<sup>-1</sup> cm<sup>-1</sup>) (Figure 2a). The ESI-MS spectrum of 1 exhibits three signals at a mass-to-charge ratio ( $m/z$ ) of 174.2, 194.7, and 406.2 (see the SI, Figure S1), corresponding to  $[Co(Me_3\text{-TPADP})(CH_3CN)]^{2+}$  (calcd  $m/z$  174.1),  $[Co(Me_3\text{-TPADP})(CH_3CN)_2]^{2+}$  (calcd  $m/z$  194.6), and  $[Co(Me_3\text{-TPADP})(ClO_4)]^+$  (calcd  $m/z$  406.1), respectively. At room temperature, 1 exhibits a magnetic

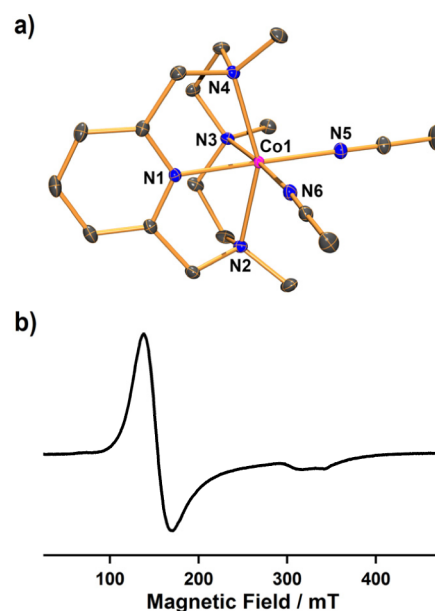


**Figure 1.** (a) ORTEP plot of  $[Co^{II}(Me_3\text{-TPADP})(CH_3CN)_2]^{2+}$  (1A) with thermal ellipsoid drawn at the 30% probability level. Hydrogen atoms are omitted for clarity. Selected bond lengths (Å): Co1–N1 2.0574(14), Co1–N2 2.1999(14), Co1–N3 2.2108(14), Co1–N4 2.2050(14), Co1–N5 2.0514(15), Co1–N6 2.1151(15). (b) X-band EPR spectrum of 1 in frozen CH<sub>3</sub>CN at 5 K. Spectroscopic settings: frequency = 9.646 GHz, microwave power = 0.998 mW, modulation frequency = 100 kHz, and modulation amplitude = 1 mT.

moment of  $4.2 \mu_B$  in CD<sub>3</sub>CN using the <sup>1</sup>H NMR Evans method consistent with the presence of three unpaired electrons,<sup>19</sup> and the X-band electron paramagnetic resonance (EPR) spectrum of 1 in CH<sub>3</sub>CN at 5 K shows an axial signal at  $g = 4.5$  and  $2.08$  (Figure 1b). These results indicate an  $S = 3/2$  ground state for 1.<sup>25</sup> In addition, the redox potential of 1 was determined as  $E_{1/2} = 0.16$  V (vs Fc<sup>+</sup>/Fc) by cyclic voltammetry (see the SI, Figure S2).<sup>26</sup>

The cobalt(III)–peroxo complex,  $[Co^{III}(Me_3\text{-TPADP})(O_2)]^+$  (2), was prepared by adding 10 equiv of hydrogen peroxide (H<sub>2</sub>O<sub>2</sub>) to a reaction solution containing 1 in the presence of 2 equiv of triethylamine (TEA) in CH<sub>3</sub>CN at 25 °C (Scheme 2), where the color of the solution changed from purple to blue. Complex 2 could not be isolated due to its thermal instability; however, it was generated and characterized at low temperature in solution. The UV–vis spectrum of 2 in CH<sub>3</sub>CN at –40 °C shows an intense absorption band at 338 nm ( $\epsilon = 2400$  M<sup>-1</sup> cm<sup>-1</sup>) and a weak absorption band at 550 nm ( $\epsilon = 230$  M<sup>-1</sup> cm<sup>-1</sup>) (Figure 2a). The ESI-MS spectrum of 2 exhibits a prominent signal at  $m/z$  339.2 (Figure 2b), whose mass and isotope distribution pattern correspond to  $[Co(Me_3\text{-TPADP})(O_2)]^+$  (calcd  $m/z$  339.1) (see the SI, Figure S3). When the reaction was carried out with isotopically labeled H<sub>2</sub><sup>18</sup>O<sub>2</sub>, a mass peak corresponding to  $[Co(Me_3\text{-TPADP})(^{18}O_2)]^+$  appeared at  $m/z$  343.2 (calcd  $m/z$  343.1) (Figure 2b, inset). The four mass unit shift upon the substitution of <sup>16</sup>O with <sup>18</sup>O indicates that 2 has two oxygen atoms.

The resonance Raman spectrum of 2 was collected using 355 nm excitation in CH<sub>3</sub>CN at –30 °C. Compound 2 prepared with H<sub>2</sub><sup>16</sup>O<sub>2</sub> exhibits an isotope-sensitive band at 888 cm<sup>-1</sup>, which shifts to 842 cm<sup>-1</sup> when H<sub>2</sub><sup>18</sup>O<sub>2</sub> is used (Figure 2a, inset, see the SI, Figure S4). The observed isotopic shift of its  $^{16}\Delta - ^{18}\Delta$  value of 46 cm<sup>-1</sup> is in agreement with the calculated value

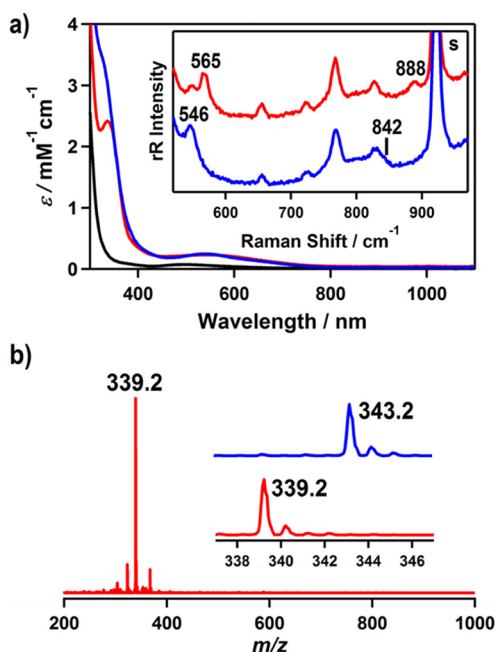


**Figure 2.** (a) UV-vis spectra of  $[\text{Co}^{\text{III}}(\text{Me}_3\text{-TPADP})(\text{CH}_3\text{CN})_2]^{2+}$  (1) (black line),  $[\text{Co}^{\text{III}}(\text{Me}_3\text{-TPADP})(\text{O}_2)]^+$  (2) (red line), and  $[\text{Co}^{\text{III}}(\text{Me}_3\text{-TPADP})(\text{O}_2\text{H})(\text{CH}_3\text{CN})]^{2+}$  (3) (blue line) in  $\text{CH}_3\text{CN}$  at  $-30^\circ\text{C}$ . Inset shows the resonance Raman spectra of 2 prepared with  $\text{H}_2^{16}\text{O}_2$  (red line) and  $\text{H}_2^{18}\text{O}_2$  (blue line) obtained upon excitation at 355 nm in  $\text{CH}_3\text{CN}$  at  $-30^\circ\text{C}$ . (b) ESI-MS of 2 in  $\text{CH}_3\text{CN}$  at  $-40^\circ\text{C}$ . Insets show the observed isotope distribution patterns for  $[\text{Co}(\text{Me}_3\text{-TPADP})(^{16}\text{O}_2)]^+$  (lower) and  $[\text{Co}(\text{Me}_3\text{-TPADP})(^{18}\text{O}_2)]^+$  (upper).

of 51  $\text{cm}^{-1}$  for the O–O harmonic oscillator. This value is comparable to those reported for structurally and spectroscopically characterized side-on cobalt(III)–peroxo complexes, such as  $[\text{Co}^{\text{III}}(12\text{-TMC})(\text{O}_2)]^+$  (902  $\text{cm}^{-1}$ ) and  $[\text{Co}^{\text{III}}(13\text{-TMC})(\text{O}_2)]^+$  (902  $\text{cm}^{-1}$ ).<sup>8e</sup> In addition, the Co–O<sub>2</sub> symmetric stretch of 2 was observed at 565  $\text{cm}^{-1}$ , which shifts to 546  $\text{cm}^{-1}$  upon  $^{18}\text{O}$ -substitution ( $^{16}\Delta - ^{18}\Delta = 19 \text{ cm}^{-1}$ ;  $^{16}\Delta - ^{18}\Delta_{(\text{calcd})} = 21 \text{ cm}^{-1}$ ) (Figure 2a, inset, see the SI, Figure S4).

The X-band EPR spectrum of 2 is silent at 4.3 K, suggesting either a low-spin ( $S = 0$ ) or an integer-spin ( $S = 1$  or 2) Co(III)  $d^6$  species. The  $^1\text{H}$  NMR spectrum of 2 recorded in  $\text{CD}_3\text{CN}$  at  $-40^\circ\text{C}$  exhibits sharp features in the 0–10 ppm region (data not shown), indicating that 2 is in a low-spin ( $S = 0$ ) state.

Addition of 3 equiv of perchloric acid ( $\text{HClO}_4$ ) to a solution containing 2 in  $\text{CH}_3\text{CN}$  at  $-20^\circ\text{C}$  immediately produced an EPR silent magenta intermediate 3 with electronic absorption bands at  $\sim 330 \text{ nm}$  ( $\epsilon = 3300 \text{ M}^{-1} \text{ cm}^{-1}$ ) and 528 nm ( $\epsilon = 240 \text{ M}^{-1} \text{ cm}^{-1}$ ) (Figure 2a). Compound 3 is thermally unstable. Even at  $-40^\circ\text{C}$ , the characteristic absorption bands of 3 decayed over the course of hours (18% decay for 1 h). The decay of 3 obeyed first-order reaction kinetics, and activation parameters,  $\Delta H^\ddagger = -115.9 \text{ kcal mol}^{-1}$  and  $\Delta S^\ddagger = -15.7 \text{ cal mol}^{-1} \text{ K}^{-1}$ , are obtained by the Eyring plot between 283 and 313 K (Figure S5). Compound 3 could not be formed via simple oxidation of 1 with excess  $\text{H}_2\text{O}_2$ . The ESI-MS spectrum of the solution at  $-40^\circ\text{C}$  suggested the formation of Co(III)–hydroperoxo species,  $[\text{Co}(\text{Me}_3\text{-TPADP})(\text{O}_2\text{H})(\text{CH}_3\text{CN})]^{2+}$  at  $m/z$  190.7 (calcd  $m/z$  190.6) and  $[\text{Co}(\text{Me}_3\text{-TPADP})(\text{O}_2\text{H})(\text{ClO}_4)]^+$  at  $m/z$  439.2 (calcd  $m/z$  439.1) (Figure 3a, see the SI, Figure S6), together with some unidentified species due to the thermal instability of 3 (see the SI, Figure S7). When the reaction was carried out with 2 prepared with isotopically

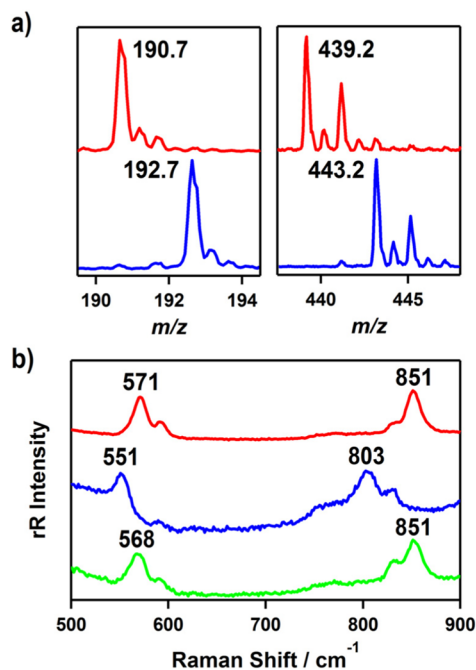


**Figure 3.** (a) ESI-MS spectra of  $[\text{Co}^{\text{III}}(\text{Me}_3\text{-TPADP})(\text{O}_2\text{H})(\text{CH}_3\text{CN})]^{2+}$  (3) in  $\text{CH}_3\text{CN}$  at  $-40^\circ\text{C}$ , which show the observed isotope distribution patterns for  $[\text{Co}(\text{Me}_3\text{-TPADP})(^{16}\text{O}_2\text{H})(\text{CH}_3\text{CN})]^{2+}$  (red line, left),  $[\text{Co}(\text{Me}_3\text{-TPADP})(^{18}\text{O}_2\text{H})(\text{CH}_3\text{CN})]^{2+}$  (blue line, left),  $[\text{Co}(\text{Me}_3\text{-TPADP})(^{16}\text{O}_2\text{H})(\text{ClO}_4)]^+$  (red line, right), and  $[\text{Co}(\text{Me}_3\text{-TPADP})(^{18}\text{O}_2\text{H})(\text{ClO}_4)]^+$  (blue line, right). (b) Resonance Raman spectra of 3 (16 mM) prepared with  $^{16}\text{O}$  (red line) and  $^{18}\text{O}$  (blue line) labeled samples of 2 obtained upon excitation at 355 nm in  $\text{CH}_3\text{CN}$  at  $-30^\circ\text{C}$ . Green line shows the spectrum of 3 prepared with a  $^{16}\text{O}$  labeled sample of 2 and  $\text{HClO}_4$  diluted in  $\text{D}_2\text{O}$ .

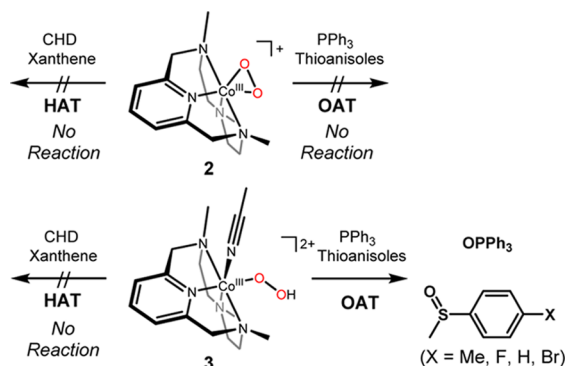
labeled  $\text{H}_2^{18}\text{O}_2$ , the mass peaks corresponding to 3 shifted to  $m/z$  192.7 for  $[\text{Co}(\text{Me}_3\text{-TPADP})(^{18}\text{O}_2\text{H})(\text{CH}_3\text{CN})]^{2+}$  (calcd  $m/z$  192.6) and 443.2 for  $[\text{Co}(\text{Me}_3\text{-TPADP})(^{18}\text{O}_2\text{H})(\text{ClO}_4)]^+$  (calcd  $m/z$  443.1) (Figure 3a). Intermediate 3 reverted back to 2 on addition of 3 equiv of TEA. The addition of  $\text{HClO}_4$  to the resulting solution regenerated 3, suggesting that 2 and 3 can be readily interconverted by the acid–base reaction depicted in Scheme 2. Such chemistry is well-known for other metal-based peroxo and hydroperoxo systems.<sup>16,27a,28,29</sup>

The resonance Raman spectrum of 3, obtained upon 355 nm excitation in  $\text{CH}_3\text{CN}$  at  $-30^\circ\text{C}$ , exhibits an isotope-sensitive band at 851  $\text{cm}^{-1}$  which shifted to 803  $\text{cm}^{-1}$  upon  $^{18}\text{O}$ -substitution (Figure 3b). The observed isotopic shift of its  $^{16}\Delta - ^{18}\Delta$  value of 48  $\text{cm}^{-1}$  is in good agreement with the calculated value of 49  $\text{cm}^{-1}$  for the O–O harmonic oscillator. The observed O–O frequency at 851  $\text{cm}^{-1}$  is comparable to that of a low-spin bleomycin–Co(III)–hydroperoxo complex (828  $\text{cm}^{-1}$ ).<sup>7h</sup> The Co–O vibrational frequency of 3 was observed at 571  $\text{cm}^{-1}$ , which shifts to 551  $\text{cm}^{-1}$  on  $^{18}\text{O}$ -substitution ( $^{16}\Delta - ^{18}\Delta = 20 \text{ cm}^{-1}$ ;  $^{16}\Delta - ^{18}\Delta_{(\text{calcd})} = 26 \text{ cm}^{-1}$ ) (Figure 3b). In order to support the formation of a hydroperoxide ligand in 3, we performed additional isotope labeling experiments. Upon  $^2\text{H}$ -substitution in 3, the 571  $\text{cm}^{-1}$  feature exhibited a 3  $\text{cm}^{-1}$  downshift (Figure 3b). The result is quite similar to those of previously reported Fe(III)–O<sub>2</sub>H species.<sup>7g,30</sup> This deuterium isotope effect supports the presence of a hydroperoxide ligand. The  $^2\text{H}$ -substitution in 3 was further confirmed by ESI-MS (see the SI, Figure S7, inset).

The  $^1\text{H}$  NMR spectrum of **3** recorded in  $\text{CD}_3\text{CN}$  at  $-40^\circ\text{C}$  shows sharp features in the 0–10 ppm region (data not shown), indicating that **3** is a low-spin Co(III)  $d^6$  species. On the basis of the spectroscopic data presented above, intermediate **3** is assigned as a low-spin Co(III)–hydroperoxo complex.

**Reactivity.** The reactivity of **2** and **3** has been investigated in electrophilic reactions: oxygen atom transfer (i.e., the oxidation of triphenylphosphine ( $\text{PPh}_3$ ) and thioanisole) and hydrogen atom transfer (i.e., the oxidation of xanthene and cyclohexadiene (CHD)) reactions (Scheme 3). Upon addition

**Scheme 3.** Overall Reactivity of **2** and **3** in Electrophilic Reactions (e.g., HAT and OAT)



of the substrates to the solution of **2** in  $\text{CH}_3\text{CN}$  at  $-20$  and  $-40^\circ\text{C}$ , the intermediate remained intact and product analysis of the reaction solution did not show oxygenated products (see the SI, Figure S8).

Unlike **2**, addition of  $\text{PPh}_3$  to a solution of **3** in  $\text{CH}_3\text{CN}$  at  $-20^\circ\text{C}$  shows the disappearance of the characteristic absorption band of **3** with a pseudo-first-order decay (see the SI, Figure S9). Product analysis of the reaction solution revealed the formation of triphenylphosphine oxide in a quantitative yield. Kinetic studies of **3** with thioanisole under the same reaction conditions also exhibit a pseudo-first-order reaction profile (Figure 4a, see the SI, Figure S10), and the first-order rate constants increased proportionally with the substrate concentration ( $k_2 = 6.7(8) \times 10^{-1} \text{ M}^{-1} \text{ s}^{-1}$ ) (Figure 4b). The rates were dependent on reaction temperature, where a linear Eyring plot was obtained between 233 and 263 K to give the activation parameters of  $\Delta H^\ddagger = 4.2 \text{ kcal mol}^{-1}$  and  $\Delta S^\ddagger = -49.4 \text{ cal mol}^{-1} \text{ K}^{-1}$  (Figure 4c). The product analysis of the reaction solution of the oxidation of thioanisole by **3** revealed that methyl phenyl sulfoxide was produced with a yield of  $75 \pm 8\%$ , and the oxygen source of the product was found to be the hydroperoxo ligand of **3** on the basis of an  $^{18}\text{O}$  labeling experiment performed with  $^{18}\text{O}$  labeled **3** (see the SI, Figure S11). In addition,  $[\text{Co}^{\text{III}}(\text{Me}_3\text{-TPADP})(\text{OH})(\text{CH}_3\text{CN})]^{2+}$  was found in the reaction solution as a decomposed product of **3** (see the SI, Figure S12). The FT-IR spectrum of the Co(III)–OH product obtained via precipitation had a peak at  $3500 \text{ cm}^{-1}$ , which is consistent with an O–H vibration.<sup>31</sup> The reactivity of **3** was further examined with *para*-substituted thioanisoles, *para*-X-Ph-SCH<sub>3</sub> (X = Me, F, H, Cl, Br), to investigate the electronic effect of *para*-substituents on the oxidation of thioanisoles by **3** (Figure 4d). The Hammett plot of the pseudo-first-order rate constants versus  $\sigma_p^+$  gave a  $\rho$  value of  $-3.6(6)$ . The negative  $\rho$  value indicates the electrophilic character of **3** in OAT reactions. Product analyses

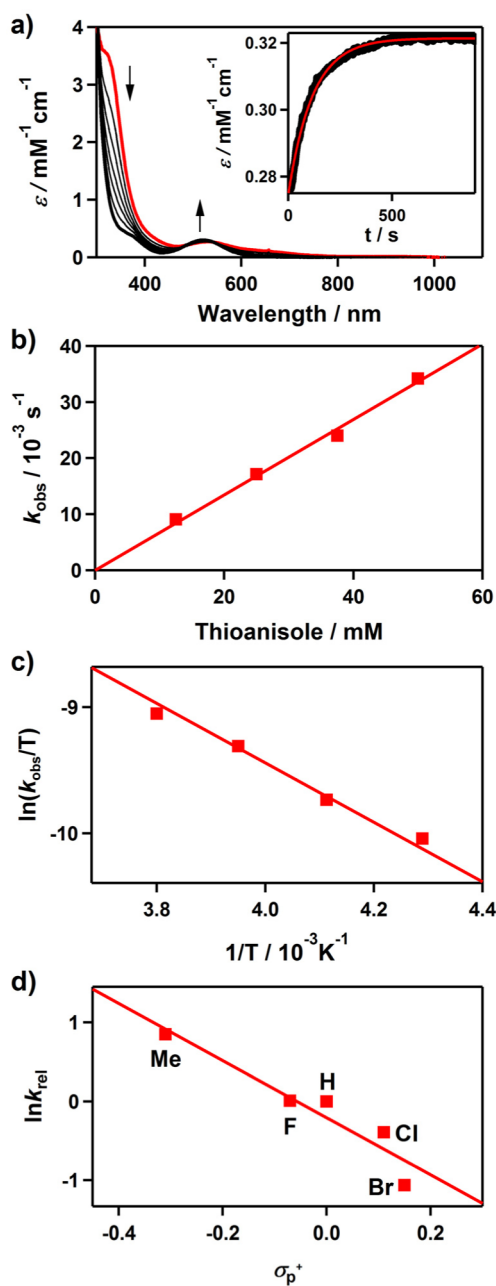


**Figure 4.** Reactions of  $[\text{Co}^{\text{III}}(\text{Me}_3\text{-TPADP})(\text{O}_2\text{H})(\text{CH}_3\text{CN})]^{2+}$  (**3**) with thioanisole in  $\text{CH}_3\text{CN}$ . (a) UV–vis spectral changes of **3** (0.5 mM) upon addition of 25 equiv of thioanisole at  $-40^\circ\text{C}$ . Inset shows the time course of the absorbance at 523 nm and its first-order fitting (red line). (b) Plot of  $k_{\text{obs}}$  against thioanisole concentration to determine a second-order rate constant for **3** at  $-40^\circ\text{C}$ . (c) Plot of pseudo-first-order rate constants against  $1/T$  to determine activation parameters for the reaction of **3** (0.5 mM) and 50 equiv of thioanisole. (d) Hammett plot of  $\ln k_{\text{rel}}$  against  $\sigma_p^+$  of *para*-substituted thioanisoles. The  $k_{\text{rel}}$  values were calculated by dividing  $k_{\text{obs}}$  of *para*-X-Ph-SCH<sub>3</sub> (X = Me, F, H, Cl, Br) by  $k_{\text{obs}}$  of thioanisole at  $-40^\circ\text{C}$ .

of the final reaction mixture revealed the formation of *para*-substituted methyl phenyl sulfoxides. It should be noted that there is a proton effect on the reactivity of **3** in the sulfoxidation reaction (see the SI, Figure S13). This result is in sharp contrast with the reactivity of  $[\text{Fe}^{\text{III}}(\text{TMC})(\text{O}_2\text{H})]^{2+}$ , where no significant proton effect was observed.<sup>27c</sup> The origin of such a proton effect remains to be established in future experiments.

It is worth noting that **3** is not capable of performing HAT reactions (data not shown). However, the reactivity of  $[\text{Fe}^{\text{III}}(\text{TMC})(\text{O}_2\text{H})]^{2+}$  in both OAT and HAT reactions has previously been reported.<sup>27b</sup> One possible explanation for the different reactivity of metal(III)–hydroperoxo species is the inability of cobalt to access its high-valent state. DFT calculations for thermodynamics of O–O homolysis for **3** relative to a low-spin Fe(III) analogue provide significant insight into their difference in reactivity (*vide supra*).

**Density Functional Theory Studies.** In a previous study evaluating the HAT reactivity of the low-spin Fe(III)–hydroperoxo complex  $[\text{Fe}^{\text{III}}(\text{N}_4\text{Py})(\text{O}_2\text{H})]^{2+}$ , it was found that the barrier for HAT was mostly due to homolysis of the O–O bond.<sup>27d</sup> In the  $\text{Me}_3\text{-TPADP}$  ligand system in this study, the Fe(III)–hydroperoxo complex is too unstable to be isolated for experimental evaluation. To calibrate this ligand set to the  $[\text{Fe}^{\text{III}}(\text{N}_4\text{Py})(\text{O}_2\text{H})]^{2+}$  results for correlation to **3**, DFT calculations were performed on the hypothetical  $[\text{Fe}^{\text{III}}(\text{Me}_3\text{-TPADP})(\text{O}_2\text{H})(\text{CH}_3\text{CN})]^{2+}$  complex to determine the thermodynamics of O–O bond homolysis relative to the results for the low-spin  $[\text{Fe}^{\text{III}}(\text{N}_4\text{Py})(\text{O}_2\text{H})]^{2+}$  complex, which were supported by experiment.<sup>7g,27d</sup> The calculated  $\Delta H$  of O–O homolysis for the  $\text{Me}_3\text{-TPADP}$  on the  $S = 1/2$  surface is 23.2 kcal mol<sup>-1</sup>, compared to 23.1 kcal mol<sup>-1</sup> previously reported for  $\text{N}_4\text{Py}$ , and the  $\Delta G$  for  $\text{Me}_3\text{-TPADP}$  was found to be 13.0 kcal mol<sup>-1</sup>, compared to 12.7 kcal mol<sup>-1</sup> for  $\text{N}_4\text{Py}$ . In the  $\text{Me}_3\text{-TPADP}$  case, as in the  $\text{N}_4\text{Py}$  case, the final products are an  $S = 1 \text{ Fe}^{\text{IV}}=\text{O}$  and an hydroxyl radical. Given the good agreement between the present set of calculations and those previously reported,<sup>7g</sup> these calculations were extended to the Co(III)–hydroperoxo complex **3**.

The geometry of **3** was optimized on the  $S = 0$ ,  $S = 1$ , and  $S = 2$  surfaces. The relative energies of these structures are given on the left of Figure 5. The lowest-energy structure for **3** was

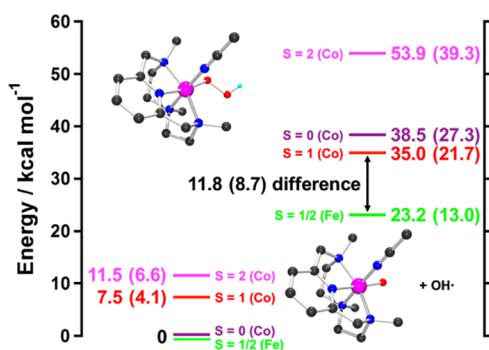


**Figure 5.** Thermodynamics of O–O homolysis for **3** on the  $S = 0$  (violet line),  $S = 1$  (red line), and  $S = 2$  (magenta line) surfaces, as well as for the Fe analogue on the  $S = 1/2$  (green line) surface. Energies are given as enthalpies, with Gibbs free energy at 298.15 K in parentheses. Homolysis of the O–O bond is 8.7 kcal mol<sup>-1</sup> more unfavorable for **3** relative to the iron complex. Insets show the geometry optimized structures of **3** (upper) and  $[\text{Co}^{\text{IV}}(\text{Me}_3\text{-TPADP})(\text{O})(\text{CH}_3\text{CN})]^{2+}$  (lower) (black, C; blue, N; cyan, H; red, O; pink, Co).

found to be  $S = 0$ , consistent with the <sup>1</sup>H NMR data (*vide supra*); thus, we focus on the  $S = 0$  calculation. Relevant geometric and vibrational parameters calculated for **3**, as well as those for its iron analogue, are presented in Table 1. The structures are similar, with the main difference being the calculated M–O bond length, which is 1.88 Å for **3** and 1.80 Å for the hypothetical iron analogue. This difference arises due to

**Table 1.** Calculated Geometric and Vibrational Parameters for **3** and Its  $S = 1/2 \text{ Fe}^{\text{III}}\text{-O}_2\text{H}$  Analogue

complex	<b>3</b>	$S = 1/2 \text{ Fe}^{\text{III}}\text{-O}_2\text{H}$
M–O (Å)	1.88	1.80
O–O (Å)	1.44	1.44
M–O–O (deg)	117	117
M–L <sub>equatorial,av</sub> (Å)	2.03	2.05
$\nu(\text{M}-(\text{O}_2\text{H}))$ (cm <sup>-1</sup> )	555	621
$\nu(\text{O}-\text{O})$ (cm <sup>-1</sup> )	928	888

the additional electron in the Co(III) relative to the low-spin Fe(III) complex, which occupies a metal d orbital  $\pi$  antibonding with the hydroperoxide. The calculated  $\nu(\text{Co}-(\text{O}_2\text{H}))$  is 555 cm<sup>-1</sup>, in agreement with the experimental value of 571 and 66 cm<sup>-1</sup> lower in energy than the corresponding calculated stretch in the iron analogue, consistent with the longer Co–O bond length. The calculated  $\nu(\text{O}-\text{O})$  is 928 cm<sup>-1</sup>, which overestimates the experimental value of 851 cm<sup>-1</sup> by 77 cm<sup>-1</sup>. A similar disagreement between calculation and experiment was observed in the previous study on the low-spin  $[\text{Fe}^{\text{III}}(\text{N}_4\text{Py})(\text{O}_2\text{H})]^{2+}$  complex,<sup>7g</sup> where an equivalent DFT calculation overestimated the experimental  $\nu(\text{O}-\text{O})$  by 98 cm<sup>-1</sup>. This was attributed to the calculations underestimating the donation from hydroperoxy  $\sigma$  and  $\pi$  bonding orbitals to the metal. Given the similarity between the present DFT calculations for **3** and the previous experimentally calibrated calculations for  $[\text{Fe}^{\text{III}}(\text{N}_4\text{Py})(\text{O}_2\text{H})]^{2+}$ , these calculations for **3** were used to evaluate the thermodynamics of its O–O bond homolysis. The enthalpies and Gibbs free energies of the O–O homolysis products of **3** on the  $S = 0$ ,  $S = 1$ , and  $S = 2$  surfaces are presented on the right-hand side of Figure 5. The  $S = 2$  products are uphill by  $\Delta G = 39.3$  kcal mol<sup>-1</sup> and are discounted. The  $S = 1$  and  $S = 0$  products are at 21.7 and 27.3 kcal mol<sup>-1</sup> in Gibbs free energy and correspond to  $S = 3/2 \text{ Co}^{\text{IV}}=\text{O}$  and  $S = 1/2 \text{ Co}^{\text{IV}}=\text{O}$  complexes, respectively, antiferromagnetically aligned to the  $S = 1/2$  hydroxyl radical. Figure 5 also presents the energetics of O–O homolysis for the iron analogue of **3**, which is  $\sim 9$  kcal mol<sup>-1</sup> more favorable than the lowest-energy O–O homolysis pathway for **3**. Note that this pathway would further require a crossover from the  $S = 0$  to the  $S = 1$  surface.

To understand the difference in O–O homolysis energy for **3** relative to its iron analogue, the electronic structures of the  $\text{M}^{\text{IV}}=\text{O}$  reaction products were analyzed, and are summarized in Figure S14 in the SI. Geometric parameters, as well as Mayer bond orders, for the products are presented in Table S3 in the SI. An  $S = 1 \text{ Fe}^{\text{IV}}=\text{O}$  has one  $\sigma$  bond between Fe and O from  $d_z^2$  interacting with the oxo  $p_z$  orbital, and one net Fe–O  $\pi$  bond from  $d_{xz}$  and  $d_{yz}$  interacting with the oxo  $p_x$  and  $p_y$ , respectively. In going from an  $S = 1 \text{ Fe}^{\text{IV}}=\text{O}$  to an  $S = 1/2 \text{ Co}^{\text{IV}}=\text{O}$  complex, an M–O  $\pi$  bonding interaction is lost through addition of an electron to the  $d_{xz}$  orbital, which has a  $\pi^*$  interaction with the O  $p_x$  orbital (see the SI, Figure S14, bottom to upper left), leading to a weaker Co–O relative to Fe–O bond. This additional  $\pi^*$  interaction is reflected both in its longer bond length (1.79 vs 1.64 Å) and lower Mayer bond order (1.14 vs 1.39). This weaker Co–O bond destabilizes the  $S = 1/2 \text{ Co}^{\text{IV}}=\text{O}$  complex relative to the  $S = 1 \text{ Fe}^{\text{IV}}=\text{O}$ . The homolysis to form this  $\text{Co}^{\text{IV}}=\text{O}$  product is 14.3 kcal mol<sup>-1</sup> higher in energy than the comparable homolysis reaction for Fe ( $27.3$  vs  $13.0$  kcal mol<sup>-1</sup>). For the lower energy  $S = 3/2 \text{ Co}^{\text{IV}}=\text{O}$  case, the extra electron relative to  $\text{Fe}^{\text{IV}}=\text{O}$   $S = 1$  is instead

added to the  $d_{x^2-y^2}$  orbital (see the SI, Figure S14, bottom to upper right), which is  $\sigma$  antibonding to the equatorial ligands. In this case, the Co–O bond is not perturbed by the additional electron, and is in fact stronger than the Fe–O bond, as reflected in its shorter bond length (1.62 Å vs 1.64 Å for  $\text{Fe}^{\text{IV}}=\text{O}$ ) and higher Mayer bond order (1.85 vs 1.39). This is due to the greater  $Z_{\text{eff}}$  on  $\text{Co}^{\text{IV}}$  relative to  $\text{Fe}^{\text{IV}}$ , which stabilizes its d manifold and allows stronger mixing with the oxygen p orbitals. However, the equatorial Co–L bonds are greatly weakened relative to those of the iron complex (see the SI, Table S3; the average  $\text{M}-\text{L}_{\text{equatorial}}$  bond increases to 2.17 from 2.07 Å, and the total Mayer bond order for these bonds decreases to 1.74 from 2.16). This overcomes the stronger Co–O bonding interaction and results in an  $S = 3/2$   $\text{Co}^{\text{IV}}=\text{O}$  that is less stable than the  $S = 1$   $\text{Fe}^{\text{IV}}=\text{O}$  by 9 kcal mol<sup>-1</sup>. Note that the  $\text{Co}^{\text{III}}-\text{O}_2\text{H}$  is also less stable than the  $\text{Fe}^{\text{III}}-\text{O}_2\text{H}$  due to weakened  $\text{M}-\text{O}_2\text{H}$  bonding arising from the additional  $d\pi^*$  electron, but this involves loss of a relatively weak  $\pi$  bonding interaction (*vide supra*; also see differences in calculated  $\text{M}-\text{O}$  bond lengths and stretching frequencies in Table 1). Thus, **3** is much less reactive than equivalent low-spin  $\text{Fe}(\text{III})$ –hydroperoxo complexes due to the higher barrier for O–O bond homolysis resulting from the additional electron in an equatorial  $\sigma$  antibonding orbital of the  $\text{Co}^{\text{IV}}=\text{O}$   $S = 3/2$  product.

## CONCLUSIONS

The metal–hydroperoxo intermediates in organic functionalizations are of current interest in enzymatic processes, pharmaceutical research, and industrial catalysis. We have synthesized mononuclear cobalt(III)–peroxo (**2**) and –hydroperoxo (**3**) complexes bearing a common macrocyclic  $\text{Me}_3\text{-TPADP}$  ligand, where **3** was prepared by protonation of **2**. The consecutive interconversion of **3** to **2** by addition of a base supports acid–base chemistry. The intermediates were characterized with a variety of physicochemical methods. Although the UV–vis spectra of **2** and **3** are not very different, ESI-MS spectra of **2** clearly exhibit the formation of the cobalt(III)–peroxo adduct at low temperature, and resonance Raman spectra of **3** show an O–O stretching vibration at 851 cm<sup>-1</sup> for <sup>16</sup>O samples (803 cm<sup>-1</sup> for <sup>18</sup>O samples), which is assignable to that of hydroperoxo species. The reactivities of **2** and **3** were compared in electrophilic reactions; **3** is capable of conducting OAT reactions, whereas **2** exhibits no OAT reactivity. Alternatively, **3** does not perform HAT, whereas low-spin  $\text{Fe}(\text{III})$ –hydroperoxo complexes do. DFT calculations show that this is due to the high O–O bond homolysis energy relative to that of the iron analogue. This energy difference is due to the additional electron in an antibonding orbital that would destabilize a high-valent Co–oxo product.

## ASSOCIATED CONTENT

### Supporting Information

The Supporting Information is available free of charge on the ACS Publications website at DOI: 10.1021/acs.inorgchem.6b02288.

Experimental details, Figures S1–S14, and Tables S1–S3 (PDF)

Crystallographic details (CIF)

## AUTHOR INFORMATION

### Corresponding Authors

\*E-mail: edward.solomon@stanford.edu.

\*E-mail: jaeheung@dgist.ac.kr.

### Notes

The authors declare no competing financial interest.

## ACKNOWLEDGMENTS

J.C. at DGIST acknowledges the financial support from the NRF (2014R1A1A2056051), the Ministry of Science, ICT and Future Planning (DGIST R&D Program 16-BD-0403, KCRC 2014M1A8A1049320, and KCGRC 2016M3D3A01913243), and the Ministry of Oceans and Fisheries (Marine Biotechnology Program 20150220) of Korea. T. Og. acknowledges the support of “Strategic Young Researcher Overseas Visits Program for Accelerating Brain Circulation” and Grant-in-Aid for Scientific Research (No. 15H00960) both by JSPS. E.I.S. at Stanford University acknowledges financial support by the National Institutes of Health (Grant GM 40392).

## REFERENCES

- (1) (a) Nam, W. Dioxygen Activation by Metalloenzymes and Models. *Acc. Chem. Res.* **2007**, *40*, 465 and review articles in the special issue. (b) Ray, K.; Pfaff, F. F.; Wang, B.; Nam, W. Status of Reactive Non-Heme Metal–Oxygen Intermediates in Chemical and Enzymatic Reactions. *J. Am. Chem. Soc.* **2014**, *136*, 13942–13958.
- (2) (a) Sheldon, R. A.; Kochi, J. K. *Metal-Catalyzed Oxidations of Organic Compounds*; Academic Press: New York, 1981. (b) *The Chemistry of Peroxides*, Patai, S., Ed.; Wiley: Chichester, U.K., 1983. (c) Norman, J. A.; Pez, G. P.; Roberts, D. A. In *Oxygen Complexes and Oxygen Activation by Transition Metals*; Martel, A. E., Sawyer, D. T., Eds.; Plenum Press: New York, 1988. (d) *Organic Peroxides*; Ando, W., Ed.; Wiley: Chichester, U.K., 1992.
- (3) (a) Special issue on Metal–Dioxygen Complexes: *Chem. Rev.* **1994**, *94*, 567–856. (b) Strukul, G. Transition Metal Catalysis in the Baeyer–Villiger Oxidation of Ketones. *Angew. Chem., Int. Ed.* **1998**, *37*, 1198–1209. (c) Murahashi, S. Synthetic Aspects of Metal-Catalyzed Oxidations of Amines and Related Reactions. *Angew. Chem., Int. Ed. Engl.* **1995**, *34*, 2443–2465.
- (4) Ortiz de Montellano, P. R. *Cytochrome P450: Structure, Mechanism, and Biochemistry*, 3rd ed.; Kluwer Academic/Plenum Publishers: New York, 2005.
- (5) (a) Holm, R. H.; Solomon, E. I. Introduction: Bioinorganic Enzymology II. *Chem. Rev.* **2014**, *114*, 3367–3368 and review articles in the special issue. (b) Kovaleva, E. G.; Lipscomb, J. D. Versatility of Biological Non-heme  $\text{Fe}(\text{II})$  Centers in Oxygen Activation Reactions. *Nat. Chem. Biol.* **2008**, *4*, 186–193. (c) Ortiz de Montellano, P. R. Hydrocarbon Hydroxylation by Cytochrome P450 Enzymes. *Chem. Rev.* **2010**, *110*, 932–948. (d) McQuarters, A. B.; Wolf, M. W.; Hunt, A. P.; Lehnert, N. 1958–2014: after 56 Years of Research, Cytochrome P450 Reactivity is Finally Explained. *Angew. Chem., Int. Ed.* **2014**, *53*, 4750–4752. (e) Tolman, W. B. Editorial for the Virtual Issue on Models of Metalloenzymes. *Inorg. Chem.* **2013**, *52*, 7307–7310.
- (6) (a) Wertz, D. L.; Valentine, J. S. Nucleophilicity of Iron–Porphyrin Complexes. *Struct. Bonding (Berlin)* **2000**, *97*, 37–60. (b) Gibson, D. T.; Parales, R. E. Aromatic Hydrocarbon Dioxygenases in Environmental Biotechnology. *Curr. Opin. Biotechnol.* **2000**, *11*, 236–243. (c) Wertz, D. L.; Sisemore, M. F.; Selke, M.; Driscoll, J.; Valentine, J. S. Mimicking Cytochrome P-450 2B4 and Aromatase: Aromatization of a Substrate Analogue by a Peroxo  $\text{Fe}(\text{III})$  Porphyrin Complex. *J. Am. Chem. Soc.* **1998**, *120*, 5331–5332. (d) Goto, Y.; Wada, S.; Morishima, I.; Watanabe, Y. Reactivity of Peroxoiron(III) Porphyrin Complexes: Models for Deformylation Reactions Catalyzed by Cytochrome P-450. *J. Inorg. Biochem.* **1998**, *69*, 241–247. (e) Hashimoto, K.; Nagatomo, S.; Fujinami, S.; Furutachi, H.; Ogo, S.; Suzuki, M.; Uehara, A.; Maeda, Y.; Watanabe, Y.; Kitagawa, T. A New Mononuclear Iron(III) Complex Containing a Peroxocarbonate Ligand. *Angew. Chem., Int. Ed.* **2002**, *41*, 1202–1205. (f) Annaraj, J.; Suh, Y.; Seo, M. S.; Kim, S. O.; Nam, W. Mononuclear Nonheme Ferric-Peroxo Complex in Aldehyde Deformylation. *Chem. Commun.*

2005, 4529–4531. (g) Kovaleva, E. G.; Lipscomb, J. D. Crystal Structures of Fe<sup>2+</sup> Dioxxygenase Superoxo, Alkylperoxo, and Bound Product Intermediates. *Science* **2007**, *316*, 453–457.

(7) (a) Chow, M. S.; Liu, L. V.; Solomon, E. I. Further Insights into the Mechanism of the Reaction of Activated Bleomycin with DNA. *Proc. Natl. Acad. Sci. U. S. A.* **2008**, *105*, 13241–13245. (b) Neese, F.; Zaleski, J. M.; Loeb-Zaleski, K.; Solomon, E. I. Electronic Structure of Activated Bleomycin: Oxygen Intermediates in Heme versus Non-Heme Iron. *J. Am. Chem. Soc.* **2000**, *122*, 11703–11724. (c) Sam, J. W.; Tang, X.-J.; Peisach, J. Electrospray Mass Spectrometry of Iron Bleomycin: Demonstration that Activated Bleomycin is a Ferric Peroxide Complex. *J. Am. Chem. Soc.* **1994**, *116*, 5250–5256. (d) Westre, T. E.; Loeb, K. E.; Zaleski, J. M.; Hedman, B.; Hodgson, K. O.; Solomon, E. I. Determination of the Geometric and Electronic Structure of Activated Bleomycin Using X-ray Absorption Spectroscopy. *J. Am. Chem. Soc.* **1995**, *117*, 1309–1313. (e) Burger, R. M.; Peisach, J.; Horwitz, S. B. Activated Bleomycin. A Transient Complex of Drug, Iron, and Oxygen that Degrades DNA. *J. Biol. Chem.* **1981**, *256*, 11636–11644. (f) Hecht, S. M. The Chemistry of Activated Bleomycin. *Acc. Chem. Res.* **1986**, *19*, 383–391. (g) Lehnert, N.; Neese, F.; Ho, R. Y. N.; Que, L., Jr.; Solomon, E. I. Electronic Structure and Reactivity of Low-Spin Fe(III)–Hydroperoxo Complexes: Comparison to Activated Bleomycin. *J. Am. Chem. Soc.* **2002**, *124*, 10810–10822. (h) Rajani, C.; Kincaid, J. R.; Petering, D. H. Resonance Raman Studies of HOO–Co(III) Bleomycin and Co(III) Bleomycin: Identification of Two Important Vibrational Modes,  $\nu(\text{Co}=\text{OOH})$  and  $\nu(\text{O}=\text{OH})$ . *J. Am. Chem. Soc.* **2004**, *126*, 3829–3836.

(8) (a) Jo, Y.; Annaraj, J.; Seo, M. S.; Lee, Y.-M.; Kim, S. Y.; Cho, J.; Nam, W. Reactivity of a Cobalt(III)–Peroxo Complex in Oxidative Nucleophilic Reactions. *J. Inorg. Biochem.* **2008**, *102*, 2155–2159. (b) Hikichi, S.; Akita, M.; Moro-oka, Y. New Aspects of the Cobalt-Dioxygen Complex Chemistry Opened by Hydrotris(pyrazolyl)borate Ligands (Tp<sup>R</sup>): Unique Properties of Tp<sup>R</sup>Co-Dioxygen Complexes. *Coord. Chem. Rev.* **2000**, *198*, 61–87. (c) Rahman, A. F. M. M.; Jackson, W. G.; Willis, A. C. The First Sideways-Bonded Peroxo Complex for a Tetraamminecobalt(III) Species. *Inorg. Chem.* **2004**, *43*, 7558–7560. (d) Hu, X.; Castro-Rodriguez, I.; Meyer, K. Dioxygen Activation by a Low-Valent Cobalt Complex Employing a Flexible Tripodal N-Heterocyclic Carbene Ligand. *J. Am. Chem. Soc.* **2004**, *126*, 13464–13473. (e) Cho, J.; Sarangi, R.; Kang, H. Y.; Lee, J. Y.; Kubo, M.; Ogura, T.; Solomon, E. I.; Nam, W. Synthesis, Structural, and Spectroscopic Characterization and Reactivities of Mononuclear Cobalt(III)–Peroxo Complexes. *J. Am. Chem. Soc.* **2010**, *132*, 16977–16986. (f) Smith, T. D.; Pilbrow, J. R. Recent Developments in the Studies of Molecular Oxygen Adducts of Cobalt(II) Compounds and Related Systems. *Coord. Chem. Rev.* **1981**, *39*, 295–383.

(9) (a) Terry, N. W.; Amma, E. L.; Vaska, L. Molecular Oxygen Binding in a Monomeric Cobalt Complex. Crystal and Molecular Structure of Dioxygen–Bis[*cis*-1,2-bis(diphenylphosphino)ethylene]cobalt Tetrafluoroborate. *J. Am. Chem. Soc.* **1972**, *94*, 653–655. (b) Egan, J. W., Jr.; Haggerty, B. S.; Rheingold, A. L.; Sendlinger, S. C.; Theopold, K. H. Crystal Structure of a Side-On Superoxo Complex of Cobalt and Hydrogen Abstraction by a Reactive Terminal Oxo Ligand. *J. Am. Chem. Soc.* **1990**, *112*, 2445–2446. (c) Rodley, G. A.; Robinson, W. T. Structure of a Monomeric Oxygen-Carrying Complex. *Nature* **1972**, *235*, 438–439. (d) Gall, R. S.; Rogers, J. F.; Schaefer, W. P.; Christoph, G. G. The Structure of a Monomeric Oxygen Carrying Cobalt Complex: Dioxygen-*N,N'*-(1,1,2,2-tetramethyl)ethylenebis(3-*tert*-butylsalicylideneiminato)(1-benzylimidazole)cobalt(II). *J. Am. Chem. Soc.* **1976**, *98*, 5135–5144. (e) Tiné, M. R. Cobalt Complexes in Aqueous Solutions as Dioxygen Carriers. *Coord. Chem. Rev.* **2012**, *256*, 316–327. (f) Schaefer, W. P.; Huie, B. T.; Kurilla, M. G.; Ealick, S. E. Oxygen-Carrying Cobalt Complexes. 10. Structures of *N,N'*-Ethylenebis(3-*tert*-butylsalicylideneiminato)cobalt(II) and Its Monomeric Dioxygen Adduct. *Inorg. Chem.* **1980**, *19*, 340–344. (g) Busch, D. H.; Jackson, P. J.; Kojima, M.; Chmielewski, P.; Matsumoto, N.; Stevens, J. C.; Wu, W.; Nosco, D.; Herron, N.; Ye, N.; Warburton, P.

R.; Masarwa, M.; Stephenson, N. A.; Christoph, G.; Alcock, N. W. Dioxygen Adducts of Lacunar Cobalt(II) Cyclidene Complexes. *Inorg. Chem.* **1994**, *33*, 910–923. (h) Wang, C.-C.; Chang, H.-C.; Lai, Y.-C.; Fang, H.; Li, C.-C.; Hsu, H.-K.; Li, Z.-Y.; Lin, T.-S.; Kuo, T.-S.; Neese, F.; Ye, S.; Chiang, Y.-W.; Tsai, M.-L.; Liaw, W.-F.; Lee, W.-Z. A structurally characterized Nonheme Cobalt–Hydroperoxo Complex Derived from Its Superoxo Intermediate via Hydrogen Atom Abstraction. *J. Am. Chem. Soc.* **2016**, *14186*–14189.

(10) (a) Calvin, M.; Bailes, R. H.; Wilmarth, W. K. The Oxygen-Carrying Synthetic Chelate Compounds.<sup>1a</sup> *J. Am. Chem. Soc.* **1946**, *68*, 2254–2256. (b) Barkelew, C. H.; Calvin, M. Oxygen-Carrying Synthetic Chelate Compounds. II. The Rates of Oxygenation of the Solid Compounds<sup>1</sup>. *J. Am. Chem. Soc.* **1946**, *68*, 2257–2262. (c) Bailes, R. H.; Calvin, M. The Oxygen-Carrying Synthetic Chelate Compounds. VII. Preparation<sup>1</sup>. *J. Am. Chem. Soc.* **1947**, *69*, 1886–1893.

(11) Niederhoffer, E. C.; Timmons, J. H.; Martell, A. E. Thermodynamics of Oxygen Binding in Natural and Synthetic Dioxygen Complexes. *Chem. Rev.* **1984**, *84*, 137–203.

(12) (a) Bailey, C. L.; Drago, R. S. Utilization of O<sub>2</sub> for the Specific Oxidation of Organic Substrates with Cobalt(II) Catalysts. *Coord. Chem. Rev.* **1987**, *79*, 321–332. (b) Cho, J.; Sarangi, S.; Nam, W. Mononuclear Metal–O<sub>2</sub> Complexes Bearing Macrocyclic *N*-Tetramethylated Cyclam Ligands. *Acc. Chem. Res.* **2012**, *45*, 1321–1330.

(13) (a) Zombeck, A.; Drago, R. S.; Corden, B. B.; Gaul, J. H. Activation of Molecular Oxygen. Kinetic Studies of the Oxidation of Hindered Phenols with Cobalt–Dioxygen Complexes. *J. Am. Chem. Soc.* **1981**, *103*, 7580–7585. (b) Hamilton, D. E.; Drago, R. S.; Zombeck, A. Mechanistic Studies on the Cobalt(II) Schiff Base Catalyzed Oxidation of Olefins by O<sub>2</sub>. *J. Am. Chem. Soc.* **1987**, *109*, 374–379.

(14) Corcos, A. R.; Villanueva, O.; Walroth, R. C.; Sharma, S. K.; Bacsa, J.; Lancaster, K. M.; MacBeth, C. E.; Berry, J. F. Oxygen Activation by Co(II) and a Redox Non-Innocent Ligand: Spectroscopic Characterization of a Radical–Co(II)–Superoxide Complex with Divergent Catalytic Reactivity. *J. Am. Chem. Soc.* **2016**, *138*, 1796–1799.

(15) (a) Bayston, J. H.; Winfield, M. E. A Mononuclear Hydroperoxo Complex and Its Significance in Catalytic Oxidation Mechanisms. *J. Catal.* **1964**, *3*, 123–128. (b) Guzei, I. A.; Bakac, A. Macrocyclic Hydroperoxocobalt(III) Complex: Photochemistry, Spectroscopy, and Crystal Structure. *Inorg. Chem.* **2001**, *40*, 2390–2393. (c) Wang, W.-D.; Bakac, A.; Espenson, J. H. Oxidation and Reduction Reactions of Hydroperoxo Cobalt Macrocycles. *Inorg. Chem.* **1995**, *34*, 4049–4056.

(16) Kim, D.; Cho, J.; Lee, Y.-M.; Sarangi, R.; Nam, W. Synthesis, Characterization, and Reactivity of Cobalt(III)–Oxygen Complexes Bearing a Macrocyclic *N*-Tetramethylated Cyclam Ligand. *Chem. - Eur. J.* **2013**, *19*, 14112–14118.

(17) (a) Mirza, S. A.; Bocquet, B.; Robyr, C.; Thomi, S.; Williams, A. F. Reactivity of the Coordinated Hydroperoxo Ligand. *Inorg. Chem.* **1996**, *35*, 1332–1337. (b) Tcho, W.-Y.; Wang, B.; Lee, Y.-M.; Cho, K.-B.; Shearer, J.; Nam, W. A Mononuclear Nonheme Cobalt(III)–Hydroperoxide Complex with an Amphoteric Reactivity in Electrophilic and Nucleophilic Oxidative Reactions. *Dalton Trans.* **2016**, *45*, 14511–14515.

(18) *Purification of Laboratory Chemicals*; Armarego, W. L. F., Perrin, D. D., Eds.; Pergamon Press: Oxford, 1997.

(19) (a) Evans, D. F. 400. The Determination of the Paramagnetic Susceptibility of Substances in Solution by Nuclear Magnetic Resonance. *J. Chem. Soc.* **1959**, 2003–2005. (b) Löliger, J.; Scheffold, R. Paramagnetic Moment Measurements by NMR. A Micro Technique. *J. Chem. Educ.* **1972**, *49*, 646–647. (c) Evans, D. F.; Jakubovic, D. A. Water-Soluble Hexadentate Schiff-Base Ligands as Sequestering Agents for Iron(III) and Gallium(III). *J. Chem. Soc., Dalton Trans.* **1988**, 2927–2933.

(20) Sheldrick, G. M. *SHELXTL/PC for Windows XP, Version 6.12*; Bruker AXS Inc.: Madison, WI, 2001.

(21) Frisch, M. J.; Trucks, G. W.; Schlegel, H. B.; Scuseria, G. E.; Robb, M. A.; Cheeseman, J. R.; Scalmani, G.; Barone, V.; Mennucci,

B.; Petersson, G. A.; Nakatsuji, H.; Caricato, M.; Li, X.; Hratchian, H. P.; Izmaylov, A. F.; Bloino, J.; Zheng, G.; Sonnenberg, J. L.; Hada, M.; Ehara, M.; Toyota, K.; Fukuda, R.; Hasegawa, J.; Ishida, M.; Nakajima, T.; Honda, Y.; Kitao, O.; Nakai, H.; Vreven, T.; Montgomery, J. A., Jr.; Peralta, J. E.; Ogliaro, F.; Bearpark, M.; Heyd, J. J.; Brothers, E.; Kudin, K. N.; Staroverov, V. N.; Kobayashi, R.; Normand, J.; Raghavachari, K.; Rendell, A.; Burant, J. C.; Iyengar, S. S.; Tomasi, J.; Cossi, M.; Rega, N.; Millam, N. J.; Klene, M.; Knox, J. E.; Cross, J. B.; Bakken, V.; Adamo, C.; Jaramillo, J.; Gomperts, R.; Stratmann, R. E.; Yazyev, O.; Austin, A. J.; Cammi, R.; Pomelli, C.; Ochterski, J. W.; Martin, R. L.; Morokuma, K.; Zakrzewski, V. G.; Voth, G. A.; Salvador, P.; Dannenberg, J. J.; Dapprich, S.; Daniels, A. D.; Farkas, Ö.; Foresman, J. B.; Ortiz, J. V.; Cioslowski, J.; Fox, D. J. *Gaussian 09, Revision D.01*; Gaussian, Inc.: Wallingford, CT, 2013.

(22) Tenderholt, A. L. *QMForge, Version 2.2*; <http://qmforge.sourceforge.net>.

(23) Kieber-Emmons, M. T. *LUMO, Version 1.0.1*.

(24) Wen, J.; Geng, Z.; Yin, Y.; Wang, Z. A Mononuclear Mn<sup>2+</sup> Complex Based on a Novel Tris-(ethyl acetate) Pendant-Armed Tetraazamacrocyclic: Effect of Pyridine on Self-Assembly and Weak Interactions. *Inorg. Chem. Commun.* **2012**, *21*, 16–20.

(25) Kang, P. C.; Eaton, G. R.; Eaton, S. S. Pulsed Electron Paramagnetic Resonance of High-Spin Cobalt(II) Complexes. *Inorg. Chem.* **1994**, *33*, 3660–3665.

(26) Complexes **2** and **3** did not give reversible or quasireversible behavior in cyclic voltammetry.

(27) (a) Li, F.; Meier, K. K.; Cranswick, M. A.; Chakrabarti, M.; Van Heuvelen, K. M.; Münck, E.; Que, L., Jr. Characterization of a High-Spin Non-Heme Fe<sup>III</sup>-OOH Intermediate and Its Quantitative Conversion to an Fe<sup>IV</sup>=O Complex. *J. Am. Chem. Soc.* **2011**, *133*, 7256–7259. (b) Cho, J.; Jeon, S.; Wilson, S. A.; Liu, L. V.; Kang, E. A.; Braymer, J. J.; Lim, M. H.; Hedman, B.; Hodgson, K. O.; Valentine, J. S.; Solomon, E. I.; Nam, W. Structure and Reactivity of a Mononuclear Non-Haem Iron(III)-Peroxo Complex. *Nature* **2011**, *478*, 502–505. (c) Kim, Y. M.; Cho, K.-B.; Cho, J.; Wang, B.; Li, C.; Shaik, S.; Nam, W. A Mononuclear Non-Heme High-Spin Iron(III)-Hydroperoxo Complex as an Active Oxidant in Sulfoxidation Reactions. *J. Am. Chem. Soc.* **2013**, *135*, 8838–8841. (d) Liu, L. V.; Hong, S.; Cho, J.; Nam, W.; Solomon, E. I. Comparison of High-Spin and Low-Spin Nonheme Fe<sup>III</sup>-OOH Complexes in O–O Bond Homolysis and H-Atom Abstraction Reactivities. *J. Am. Chem. Soc.* **2013**, *135*, 3286–3299.

(28) So, H.; Park, Y. J.; Cho, K.-B.; Lee, Y.-M.; Seo, M. S.; Cho, J.; et al. Sarangi, R.; Nam, W. Spectroscopic Characterization and Reactivity Studies of a Mononuclear Nonheme Mn(III)-Hydroperoxo Complex. *J. Am. Chem. Soc.* **2014**, *136*, 12229–12232.

(29) (a) Jensen, K. B.; McKenzie, C. J.; Nielsen, L. P.; Pedersen, J. Z.; Svendsen, H. M. Deprotonation of Low-Spin Mononuclear Iron(III)-Hydroperoxide Complexes Give Transient Blue Species Assigned to High-Spin Iron(III)-Peroxide Complexes. *Chem. Commun.* **1999**, 1313–1314. (b) Ho, R. Y. N.; Roelfes, G.; Hermant, R.; Hage, R.; Feringa, B. L.; Que, L., Jr. Resonance Raman Evidence for the Interconversion between an [Fe<sup>III</sup>-η<sup>1</sup>-OOH]<sup>2+</sup> and [Fe<sup>III</sup>-η<sup>2</sup>-O<sub>2</sub>]<sup>+</sup> Species and Mechanistic Implications Thereof. *Chem. Commun.* **1999**, 2161–2162. (c) Nebe, T.; Beitat, A.; Würtele, C.; Dücker-Benfer, C.; van Eldik, R.; McKenzie, C. J.; Schindler, S. Reinvestigation of the Formation of a Mononuclear Fe(III) Hydroperoxido Complex Using High Pressure Kinetics. *Dalton Trans.* **2010**, 39, 7768–7773.

(30) (a) Roelfes, G.; Lubben, M.; Chen, K.; Ho, R. Y. N.; Meetsma, A.; Genseberger, S.; Hermant, R. M.; Hage, R.; Mandal, S. K.; Young, V. G., Jr.; Zang, Y.; Kooijman, H.; Spek, A. L.; Que, L., Jr.; Feringa, B. L. Iron Chemistry of a Pentadentate Ligand That Generates a Metastable Fe<sup>III</sup>-OOH Intermediate. *Inorg. Chem.* **1999**, *38*, 1929–1936. (b) Ho, R. Y. N.; Roelfes, G.; Feringa, B. L.; Que, L., Jr. Raman Evidence for a Weakened O–O Bond in Mononuclear Low-Spin Iron(III)-Hydroperoxides. *J. Am. Chem. Soc.* **1999**, *121*, 264–265. (c) Simaan, A. J.; Döpner, S.; Banse, F.; Bourcier, S.; Bouchoux, G.; Boussac, A.; Hildebrandt, P.; Girerd, J.-J. Fe<sup>III</sup>-Hydroperoxo and Peroxo Complexes with Aminopyridyl Ligands and the Resonance Raman Spectroscopic Identification of the Fe–O and O–O Stretching

Modes. *Eur. J. Inorg. Chem.* **2000**, *2000*, 1627–1633. (d) Mairata i Payeras, A.; Ho, R. Y. N.; Fujita, M.; Que, L., Jr. The Reaction of [Fe<sup>II</sup>(tpa)] with H<sub>2</sub>O<sub>2</sub> in Acetonitrile and Acetone-Distinct Intermediates and Yet Similar Catalysis. *Chem. - Eur. J.* **2004**, *10*, 4944–4953. (e) Ohta, T.; Liu, J.-G.; Naruta, Y. Resonance Raman Characterization of Mononuclear Heme-Peroxo Intermediate Models. *Coord. Chem. Rev.* **2013**, *257*, 407–413.

(31) (a) Bergquist, C.; Fillebeen, T.; Morlok, M. M.; Parkin, G. Protonation and Reactivity towards Carbon Dioxide of the Mononuclear Tetrahedral Zinc and Cobalt Hydroxide Complexes, [Tp<sup>But,Me</sup>]ZnOH and [Tp<sup>But,Me</sup>]CoOH: Comparison of the Reactivity of the Metal Hydroxide Function in Synthetic Analogues of Carbonic Anhydrase. *J. Am. Chem. Soc.* **2003**, *125*, 6189–6199. (b) Lucas, R. L.; Zart, M. K.; Murkerjee, J.; Sorrell, T. N.; Powell, D. R.; Borovik, A. S. A Modular Approach toward Regulating the Secondary Coordination Sphere of Metal Ions: Differential Dioxygen Activation Assisted by Intramolecular Hydrogen Bonds. *J. Am. Chem. Soc.* **2006**, *128*, 15476–15489. (c) Singh, U. P.; Babbar, P.; Tyagi, P.; Weyhermüller, T. A Mononuclear Cobalt(II) Hydroxo Complex: Synthesis, Molecular Structure, and Reactivity Studies. *Transition Met. Chem.* **2008**, *33*, 931–940.